Fumihiko Matsui*, Naoyuki Maejima, Hirosuke Matsui, Hiroaki Nishikawa, Hiroshi Daimon, Tomohiro Matsushita, Matthias Muntwiler, Roland Stania, and Thomas Greber

Circular Dichroism in Cu Resonant Auger Electron Diffraction

DOI 10.1515/zpch-2015-0665
Received July 24, 2015; accepted September 22, 2015

Abstract: Upon a core level excitation by circularly polarized light (CPL), the angular momentum of light, i.e. helicity, is transferred to the emitted photoelectron. This phenomenon can be confirmed by the parallax shift measurement of the forward focusing peak (FFP) direction in a stereograph of the atomic arrangement. The angular momentum of the emitted photoelectron is the sum of CPL helicity and the magnetic quantum number (MQN) of the initial state that define the quantum number of the core hole final state. The core hole may decay via Auger electron emission, where in this two electron process the angular momentum has to be conserved as well. Starting from a given core hole, different Auger decay channels with different final state energies and angular momenta of the emitted Auger electrons may be populated. Here we report the observation and formulation of the angular momentum transfer of light to Auger electrons, instead of photoelectrons. We measured photoelectron and Auger electron intensity angular distributions from Cu(111) and Cu(001) surfaces as a function of photon energy and photoelectron kinetic energy. By combining Auger electron spectroscopy with

***Corresponding author: Fumihiko Matsui,** Graduate School of Materials Science, Nara Institute of Science and Technology, Takayama 8916-5, Ikoma, Nara 630-0192, Japan, e-mail: matui@ms.naist.jp
Naoyuki Maejima: Nara Institute of Science and Technology, Nara 630-0192, Japan; and present affiliation: Condensed Matter Science Unit, Quantum Beam Science Center, Japan Atomic Energy Agency, Sayo, Hyogo 679-5198, Japan
Hirosuke Matsui: Nara Institute of Science and Technology, Nara 630-0192, Japan; and present affiliation: Department of Chemistry, Graduate School of Science, Nagoya University, Nagoya, Aichi 464-8602, Japan
Hiroaki Nishikawa, Hiroshi Daimon: Graduate School of Materials Science, Nara Institute of Science and Technology, Takayama 8916-5, Ikoma, Nara 630-0192, Japan
Tomohiro Matsushita: Japan Synchrotron Radiation Research Institute (JASRI), SPring-8, Koto 1-1-1, Sayo, Hyogo 679-5198, Japan
Matthias Muntwiler: Paul Scherrer Institut, CH-5232 Villigen, Switzerland
Roland Stania, Thomas Greber: Physik Institut, Zürich University, CH-8057 Zürich, Switzerland

the FFP shift measurements at absorption threshold, element- and MQN-specific hole states can be generated in the valence band.

Keywords: Photoelectron Diffraction, Auger Electron, Circular Dichroism, Atomic Orbital.

1 Introduction

Copper is nonmagnetic, while nickel, which has one less electron than copper, is ferromagnetic. Gold is chemically inert, while platinum, which has one less electron than gold, is an essential element in catalyst chemistry. If we can generate a valence hole with arbitrary atomic orbital character in the solid, excited states with new electronic properties are created, which can not be achieved by a simple thermal excitation. The Auger electron emission processes that involve two valence electrons allow e.g. for the creation of a nickel-like $3d^8 4s^2$ atom in a copper matrix. As we show here the polarization of this $3d^8 4s^2$ impurity may be controlled by the light incidence and polarization of the light that creates the core hole for the Auger decay process.

Core-level photoelectron spectroscopy and diffraction are powerful techniques to analyze element specific electronic and atomic structures, respectively [1]. Forward focusing peaks (FFPs) appearing in the photoelectron intensity angular distribution (PIAD) indicate the directions of atoms surrounding a photoelectron emitter atom [2–4]. When a core level is excited by circularly polarized light (CPL), angular momentum of light, i.e. helicity, is transferred to the emitted photoelectron, which can be confirmed by taking a stereograph of the atomic arrangement and measuring the parallax shift of FFP direction [5]. The parallax shift of FFP is proportional to the angular momentum of the emitted photoelectron and inversely proportional to the interatomic distance between the photoelectron emitter and scattering atoms. The angular momentum of the emitted photoelectron (m_f) is the summation of CPL helicity (σ) and the orbital magnetic quantum number (MQN) of the initial state (m_i). Angular circular dichroism contrasts originate from the interference of the direct wave from the emitter atom and the wave scattered by the neighboring atoms. Thus they reflect the local atomic and electronic structure.

Prominent FFP angular circular dichroism was also observed in the valence band PIADs at the high kinetic energy of around 500 eV [6, 7]. The angular shift of the photoelectron FFP for the graphite σ_{xy} bands was twice of that for the π and $2s$ bands. This indicates that the FFP shift can be used to measure the MQN of atomic orbitals constituting each of the energy bands. By setting an analyzer at the corre-

sponding FFP position, the photoelectron with a specific angular momentum can be selectively detected. Correspondingly, an orbital-momentum-polarized hole state is created.

Here we report the observation of the angular momentum transfer from the excitation light to the resonant Auger electrons resulting from the decay process filling a core hole after the core level excitation to the conduction band [8]. The angular part of the Auger electron transition matrix element is formulated for the understanding of the resonant Auger electron circular dichroism. The resonant Auger electron emission by CPL excitation is an excellent way to polarize valence bands with a specific orbital magnetic momentum and a specific atomic number in a controlled fashion localized in space and time. This is useful for revealing the contribution of each atomic orbital to the electronic properties in compound crystals and epitaxial thin films.

2 Principle

The wave function of an emitted electron with kinetic energy E and wave vector $\mathbf{k}$ is written as a partial wave expansion [9]:

$$\psi_{E,\mathbf{k}}(r,\theta,\phi) = 4\pi \sum_{lm} i^l \exp(-i\delta_l) Y^*_{lm}(\theta_k,\phi_k) Y_{lm}(\theta,\phi) R_{El}(r). \tag{1}$$

δ_l is the phase shift for the partial wave l. θ_k and ϕ_k are the polar and azimuthal angles of the outgoing direction of the emitted photoelectron with respect to the incident photon axis. $R_{El}(r)$ is the radial wave function. Here, we focus on the angular part of photoelectron and Auger electron emission processes for discussing the angular distribution of circular dichroism. We derived an intensity ratio for each final state (l_f,m_f) with the angular distribution $Y_{l_f m_f}$.

2.1 Angular momentum of the photoelectron

The Gaunt coefficient is the product of three spherical harmonics integrated over the full solid angle. It is easily derived using tabulated values of Clebsch–Gordan coefficients $C(l_1 \nu l_2; 000)$ and $C(l_1 \nu l_2; m_1 \sigma m_2)$.

$$c^\nu(l_2,m_2,l_1,m_1) = \sqrt{\frac{4\pi}{2\nu+1}} \int_0^\pi \int_0^{2\pi} \sin\theta \mathrm{d}\theta \mathrm{d}\phi Y^*_{l_2 m_2} Y_{\nu\sigma} Y_{l_1 m_1} \tag{2}$$

$$= \sqrt{\frac{2l_1+1}{2l_2+1}} C(l_1 \nu l_2; 000) C(l_1 \nu l_2; m_1 \sigma m_2) \tag{3}$$

The dipole operator ($\nu = 1$) with helicity σ is denoted by a spherical harmonics $Y_{1\sigma}$. The dipole excitation probability from an initial bound state $Y_{l_i m_i}$ to a partial wave $Y_{l_f m_f}$ of final continuum state is proportional to the square of a Gaunt coefficient $c^1(l_f, m_f, l_i, m_i)$ [9–12] and is non-zero under the following conditions:

$$\Delta l \equiv l_f - l_i = \pm 1, \tag{4}$$

$$\Delta m \equiv m_f - m_i = \sigma = 0, \pm 1. \tag{5}$$

The radial matrix element R_{l_f} is independent of MQN. The contributions of $l_i \pm 1$ channels are evaluated by taking the radial matrix element ratio R_{l_i+1}/R_{l_i-1} and phase shift $\delta_{l_i \pm 1}$ into account [9]. In the case of the angular circular dichroism evaluation consisting the different $m_i \rightarrow m_f$ transitions, the radial matrix element effect becomes simply a constant factor for each $l_i \rightarrow l_f$ transition.

The effective MQN of photoelectron $m_f^*(\theta_k)$ is the average of the different final state angular momenta m_f from the initial states of quantum number $m_i = m_f - \sigma$ weighted by the transition probability at θ_k [13]. $\Theta_{l_f m_f}$ is a polar angle part of spherical harmonics. $m_f^*(\theta_k)$ is as follows.

$$m_f^*(\theta_k) = \frac{\sum_{m_i=-l_i}^{l_i} m_f |c^1(l_f, m_f, l_i, m_i)\Theta_{l_f m_f}|^2}{\sum_{m_i=-l_i}^{l_i} |c^1(l_f, m_f, l_i, m_i)\Theta_{l_f m_f}|^2} \tag{6}$$

Figure 1(a) and (b) show the polar angle (θ_k) dependence of p to d and d to f transition probabilities. The left panels of Figure 1 summarize the final state spherical harmonics for a $l_i \rightarrow l_f = l_i + 1$ channel. The transition probability from each atomic orbital by CPL excitation is indicated. The right panel shows the effective MQN. For instance, in the case of a $p \rightarrow d$ transition, the final states of $m_f = 0$, 1, and 2 are the majority at the emission angle of 0°, 45°, and 90°, respectively, as shown in Figure 1(a). In the case of $d \rightarrow f$ transition as shown in Figure 1(b), contributions to $m_f^*(90^\circ)$ for $m_f = 0$ and 2 will be 0, while that of m_f with ±1 will be 0 at $\theta_{out} = 63.43^\circ$. By setting appropriate incident angle, photoelectron with specific angular momentum m_f can be excluded.

The photoelectron is partially scattered by the surrounding atoms. Direct and scattered waves interfere and form photoelectron diffraction patterns, and FFPs at the directions of surrounding scattering atoms. The photoelectron wave propagates perpendicular to the photoelectron isophase plane, $\exp[i(kr + m_f^*\phi)]$. The real part of a simulated Cu 3d photoelectron wave function from a Cu 9-atom cluster excited by CPL is shown in Figure 2 [14]. The center atom is the photoelectron emitter. The kinetic energy was set to 914 eV. Red and blue wave fronts correspond to direct and scattered photoelectron waves, respectively. The effective MQN of photoelectron is non-zero in the case of CPL excitation, thus the isophase plane of photoelectron direct wave is a spiral. This causes the rotation of the FFP

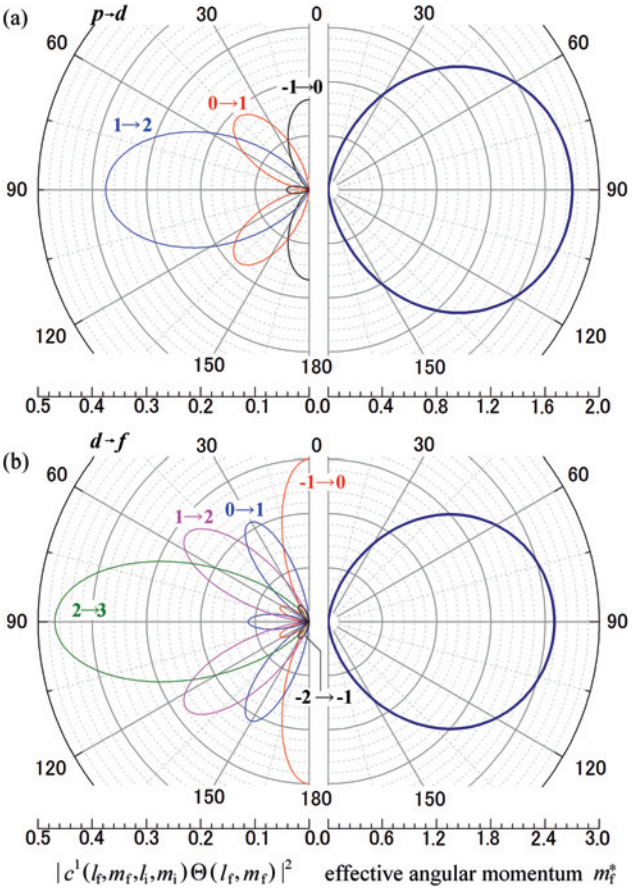

Figure 1: Left panels: Polar angle θ_k dependence of the transition probabilities from each atomic orbital by circularly polarized light excitation for (a) p to d and (b) d to f transitions. Right panels: same as left panels but for the effective angular momenta for photoelectrons.

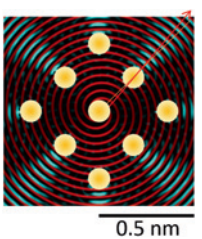

Figure 2: Real part of Cu $3d$ photoelectron wave function from a Cu 9-atom cluster excited by circularly polarized light. Center atom is photoelectron emitter. Incident photon axis is perpendicular to the cluster plane. Kinetic energy was set at 914 eV. The directions of forward focusing peaks (FFPs) shift rotationally due to angular momentum transfer from incident photon. Red and blue wave fronts correspond to the direct and scattered photoelectron waves.

direction around the incident light axis toward the same direction as the helicity of CPL. The rotation angle $\Delta\phi$ is well described by the Daimon formula [5, 15]:

$$\Delta\phi = \tan^{-1}\frac{m_{\mathrm{f}}^{*}(\theta_k)}{kR\sin^2\theta_k}, \tag{7}$$

where k is the wave number of photoelectron. The shift $\Delta\phi$ is inversely proportional to the interatomic distance R between the photoelectron emitter and the scattering atoms. Thus, the local stereoscopic atomic arrangements can be imaged directly with a stereograph which consists of a pair of PIADs excited by CPL [5, 15–17].

2.2 Angular momentum of the Auger electron

After the core-hole creation, two electrons labeled 1 and 2 and occupying ψ_{A} and ψ_{B}, take parts in the succeeding Auger electron emission process. Here, the wave functions for the core hole and the Auger electron are denoted as $\psi_{l_{\mathrm{i}}m_{\mathrm{i}}}$ and $\psi_{l_{\mathrm{f}}m_{\mathrm{f}}}$, respectively. Consequently, the Auger electron transition probability ω_{fi} is expressed as follows [18–20].

$$\omega_{\mathrm{fi}} = \hbar^{-2}|D - E|^2 \tag{8}$$

$$\text{direct: } D = \langle\psi_{l_{\mathrm{f}}m_{\mathrm{f}}}(2)\psi_{l_{\mathrm{i}},m_{\mathrm{i}}}(1)||r_1 - r_2|^{-1}|\psi_{\mathrm{A}}(1)\psi_{\mathrm{B}}(2)\rangle \tag{9}$$

$$\text{exchange: } E = \langle\psi_{l_{\mathrm{f}}m_{\mathrm{f}}}(2)\psi_{l_{\mathrm{i}},m_{\mathrm{i}}}(1)||r_1 - r_2|^{-1}|\psi_{\mathrm{A}}(2)\psi_{\mathrm{B}}(1)\rangle \tag{10}$$

Separation of the matrix element D and E into radial and angular factors is accomplished by expressing the Coulomb interaction potential in terms of products of spherical harmonics,

$$\frac{1}{|r_1 - r_2|} = \sum_{\nu\sigma}\frac{4\pi}{2\nu+1}\gamma_\nu(r_1, r_2)Y^{*}_{\nu\sigma}(r_1)Y_{\nu\sigma}(r_2), \tag{11}$$

where

$$\gamma_\nu(r_1, r_2) = r_1^{\nu}/r_2^{\nu+1}, \quad r_1 < r_2 \tag{12}$$

$$= r_2^{\nu}/r_1^{\nu+1}, \quad r_1 > r_2. \tag{13}$$

Refer to elsewhere for the radial factors [21–23]. The transition probability for $Y_{l_{\mathrm{f}}m_{\mathrm{f}}}(\theta,\phi)$ final state is the square of $d_{l_{\mathrm{f}}m_{\mathrm{f}}}$ which is the sum of Gaunt coefficient products for each spherical harmonic operator.

$$d_{l_{\mathrm{f}}m_{\mathrm{f}}} = \sum_{\nu\sigma}\frac{4\pi}{2\nu+1}\langle Y_{l_{\mathrm{f}}m_{\mathrm{f}}}|Y_{\nu\sigma}|Y_{\mathrm{B}}\rangle\langle Y_{l_{\mathrm{i}}m_{\mathrm{i}}}|Y^{*}_{\nu\sigma}|Y_{\mathrm{A}}\rangle \tag{14}$$

$$= \sum_{\nu\sigma} c^{\nu}(l_f, m_f, l_B, m_B) c^{\nu}(l_i, m_i, l_A, m_A) \tag{15}$$

$$e_{l_f m_f} = \sum_{\nu\sigma} c^{\nu}(l_f, m_f, l_A, m_A) c^{\nu}(l_i, m_i, l_B, m_B) \tag{16}$$

ν is a non-negative integer. σ is an integer between $-\nu$ and ν. In the case of direct transition, ν and σ have the following relations with quantum numbers.

$$\nu = |l_f - l_B| = |-l_i + l_A| \tag{17}$$

$$\sigma = m_f - m_B = -m_i + m_A \tag{18}$$

Note that the angular momentum (σ) released by the electron filling the core hole is transferred to the emitted Auger electron. In case of $L_{2,3}M_{4,5}M_{4,5}$ Auger electron emission, i.e., transition between $3d$ and $2p$ core levels, ν is equal to 1. This can be understood that a virtual photon emitted by the $\psi_A \rightarrow Y_{l_i m_i}$ transition triggers the $\psi_B \rightarrow Y_{l_f m_f}$ Auger electron emission transition.

In some cases, the quantum numbers (l_i, m_i) of the core-hole state can be specified by tuning the excitation photon energy at the resonance and selecting the destination conduction band state (CB) for the core-level electron by polarized light excitation. In the present case of Cu *LMM* Auger electrons, we used the resonant transition of $2p$ ($l_i = 1$) to $4s$ ($l_{CB} = 0, m_{CB} = 0$) by the CPL excitation ($\sigma = \pm 1$) to specify the MQN of initial state as $m_{CB} - \sigma = -\sigma$. Furthermore, the different two-hole final states $\psi_A\psi_B$ can be accessed individually by analyzing the corresponding Auger electron kinetic energies since the two-hole final states $\psi_A\psi_B$ are energetically separated.

Normally, the angular momentum of photon is transferred mostly to the photoelectron, however, at the absorption edge, the angular momentum is partially transferred to the resonant Auger electrons when a MQN-polarized core hole is generated [8].

3 Experimental details

The single-crystalline Cu(111) and (001) surfaces were sputtered with Ar^+ ions and annealed up to 500 °C in ultra high vacuum condition to obtain clean surfaces. The quality of the substrate surfaces was checked by electron diffraction, Cu photoelectron spectroscopy, and their angular distributions [24, 25]. No contamination was identified.

The [101] FFP intensity from the Cu(111) surface as a function of photoelectron kinetic energy and photon energy was measured using a concentric hemispherical energy analyzer at the soft x-ray beamline X03DA (Photoemission and

atomic resolution laboratory; PEARL) of Swiss Light Source (SLS). Linearly polarized light was used in the present study [26]. The emission angle relative to the incident photon axis was fixed at 60°. The sample was mounted on a 6-axis manipulator.

Cu 3*d* PIAD and *LMM* Auger electron intensity angular distribution (AIAD) from the Cu(001) surface were measured using a display-type spherical mirror analyzer (DIANA) [27, 28] at the circularly-polarized soft x-ray beamline BL25SU of SPring-8, Japan [29]. Details of PIAD data processing are described elsewhere [30]. The helicity ($\sigma = \pm 1$) of monochromatized CPL at BL25SU was reversed by switching the path of the storage ring electrons in twin helical undulators at 0.1 Hz [31]. The acceptance solid angle of the analyzer was 1π steradian (±60°). Electrons emitted from the sample were energy-analyzed, and their angular distributions were projected onto the fluorescent screen. The photon energy resolution was about 100 meV. The electron energy resolution is determined by the analyzer energy window width as indicated below for each measurement.

The photon energy of the Cu L_3 absorption threshold measured at BL25SU [8] was larger than the measurements at X03DA and the other facilities [32, 33] by about 1 eV, probably due to the technical issue of the analyzer work function evaluation for the photon energy calibration.

4 Results and discussion

4.1 Kinetic energy and photon energy mapping

We measured the nearest neighboring atom FFP intensity at the [101] direction from the Cu(111) surface as a function of photon energy and photoelectron kinetic energy at X03DA, PEARL. Figure 3(a) shows a two-dimensional intensity map. Abscissa and ordinate are photon energy and photoelectron kinetic energy, respectively. Diagonal lines where the kinetic energy increases with slope 1 with the photon energy correspond to states with constant binding energies. In the present case, valence band photoelectrons were clearly observed. By averaging the FFP intensity for various photon energies at each kinetic energy, an x-ray excited Auger electron spectrum was obtained as shown in Figure 3(b). The Cu $L_2M_{4,5}M_{4,5}$ Auger electron at a kinetic energy around 934 eV appears as a horizontal line with a constant kinetic energy starting from photon energy of 953.0 eV in Figure 3(a). The horizontal lines with a constant kinetic energy starting from a photon energy of 933.1 eV correspond to the $L_3M_{4,5}M_{4,5}$ Auger electrons. The strongest intensity peak at the kinetic energy of 914 eV and the second largest

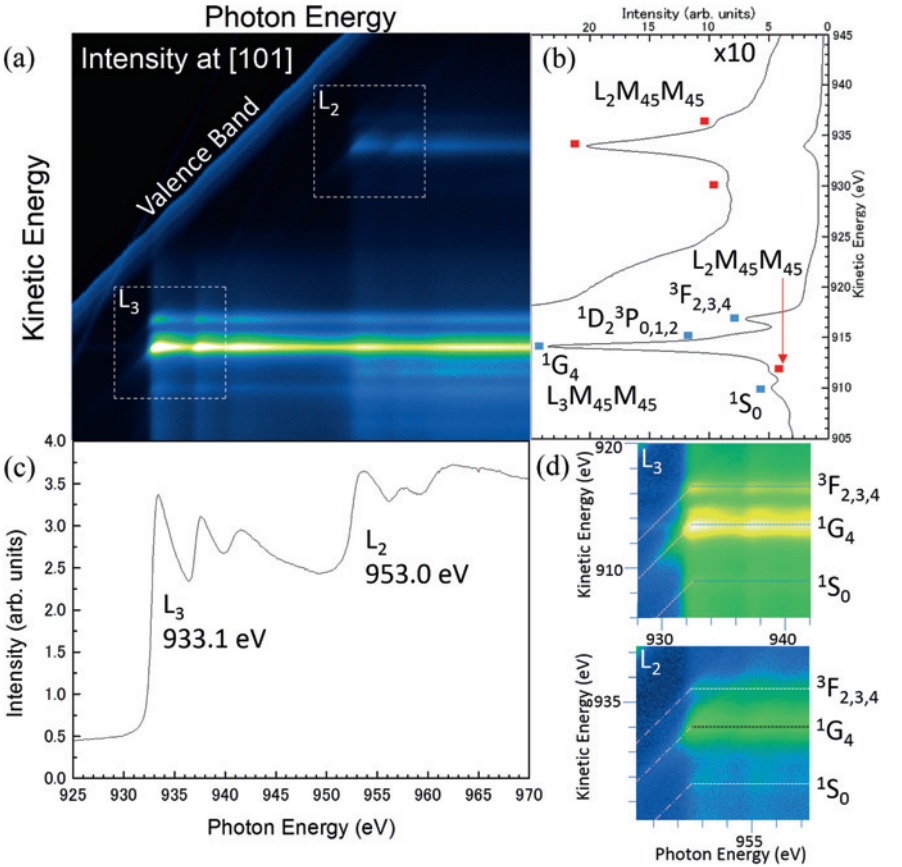

Figure 3: (a) A two-dimensional intensity map of the [101] FFP. Abscissa and ordinate are photon energy and photoelectron kinetic energy, respectively. Valence band photoelectron was observed as a diagonal line. (b) An x-ray excited Auger electron spectrum obtained by averaging the FFP intensity for various photon energies at each kinetic energy. (c) An x-ray absorption spectrum obtained by averaging the FFP intensity for various kinetic energies at each photon energy. (d) The L_3 and L_2 absorption edge region intensity mapped in a logarithm scale.

peak at 917 eV correspond to the two-hole final state of the $^1G_4$ and the $^3F_{2,3,4}$ multiplets, respectively. The $^1S_0$ multiplet peak was observed at 910 eV. The shoulder structure at 915 eV corresponds to $^1D_2$ and $^3P_{0,1,2}$ multiplets [20].

On the other hand, by averaging the FFP intensity for various kinetic energies at each photon energy, an x-ray absorption spectrum was obtained. The L_3 and L_2 absorption thresholds appear at the photon energies of 933.1 eV and 953 eV, respectively. Note that Auger-electron-like feature with a kinetic energy of 911.8 eV appeared at a photon energy above the L_2 absorption threshold but not below

the threshold. Moreover, $L_3M_{4,5}M_{4,5}$ Auger electron intensity is also enhanced at the L_2 edge. These are the effects due to $L_2L_3M_{4,5}$ Coster–Kronig transitions which has been observed [20, 34] and studied experimentally [35–37] and theoretically [21, 22, 38]. The energy difference between the 911.8-eV peak (three-hole final state) and corresponding $^3F\ L_2M_{4,5}M_{4,5}$ peak (two-hole final state) was 24.7 eV which is larger than the spin-orbital splitting of 19.9 eV. The difference of 4.8 eV is due to the difference in the two-hole and three-hole final states [39]. Figure 3(d) shows the L_3 and L_2 absorption edge region intensity map replotted in a logarithmic scale. Below the absorption thresholds, photoelectron-like resonance Raman Auger scattering effects are detected [32, 33]. The multiplet structure was also observed in the resonance Raman Auger electron spectra for the first time at the L_3 edge as well as the L_2 edge. They are connected to the corresponding Auger electron lines of $^1G_4$, $^3F_{2,3,4}$, and $^1S_0$.

4.2 Circular dichroism in angular distributions

The prominent FFP angular circular dichroism was also observed in the valence band PIADs at the high kinetic energy of around 500 eV [6]. Recently, extraordinary large angular momentum transfer to the resonant Auger electron where the excited core electron is trapped at conduction band was found by Morscher et al. [40] for Ni L_2 absorption. We reported a quantitative analysis of angular-momentum-polarized $L_3M_{4,5}M_{4,5}$ Auger electrons from a nonmagnetic Cu(001) surface at L_3 absorption threshold. Upon detection of each angular-momentum-polarized Auger electron, the element- and MQN-specific hole in valence band is generated correspondingly.

We measured full hemisphere PIAD and AIAD from the Cu(001) surface at BL25SU, SPring-8 [8]. Figure 4(a) shows a Cu valence PIAD at the kinetic energy of 914 eV. PIADs excited by both helicities ($\sigma = \pm 1$) were added. The incidence direction of CPL, i.e. the quantization axis, was aligned along the surface normal. The energy window width of DIANA was set to 5% of 914 eV and the whole valence band intensity or $L_3M_{4,5}M_{4,5}$ Auger electrons were integrated. The FFPs at the four $\langle 101 \rangle$ directions correspond to the scattering by the nearest neighbor atoms, while the center [001] direction corresponds to the second nearest neighbor atoms along the surface normal. Note that at this kinetic energy, FFP is also present even for a delocalized valence band due to the majority of the excitation coming from electron density existing at the vicinity of nucleus [6]. The FFP covers about 10° solid angle. Figure 4(b) shows a resonant Cu $L_3M_{4,5}M_{4,5}$ AIAD at the kinetic energy of 914 eV excited by CPL with photon energy of 934.2 eV.

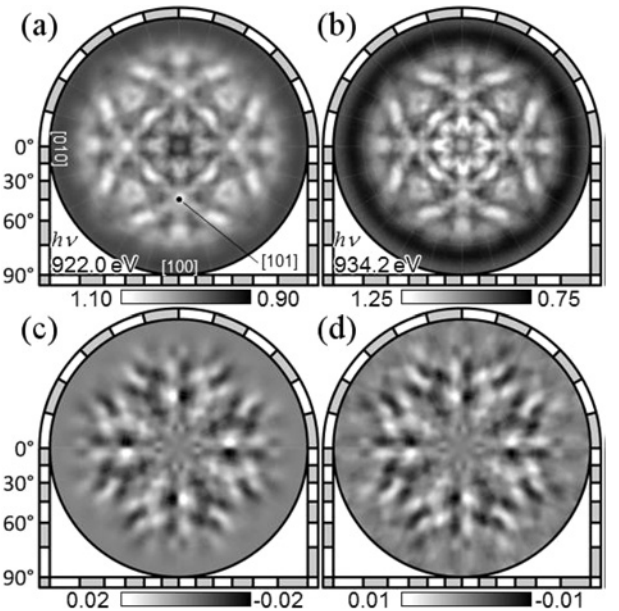

Figure 4: (a) A Cu valence PIAD at the kinetic energy of 914 eV. PIADs excited by both helicities ($\sigma = \pm 1$) were added. (b) A resonant Cu $L_3M_{4,5}M_{4,5}$ AIAD at the kinetic energy of 914 eV excited by CPL with photon energy of 934.2 eV. (c) The difference of the two valence PIADs excited by both helicities and normalized by the sum. (d) Same as (c) but for AIAD shown in (b).

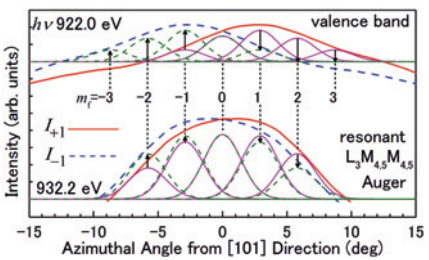

Figure 5: Azimuthal profiles of the [101] FFP intensity for valence photoelectron and Auger electrons.

Figure 4(c) shows circular dichroism angular distibution (CDAD) of the valence band, i.e. the difference of the two PIADs excited by both helicities and normalized by the sum; $(I_1 - I_{-1})/(I_1 + I_{-1})$. The suffix denotes the helicity. Figure 4(d) shows the CDAD of the resonant AIAD. This result indicates that at L_3 absorption threshold, where the excited core electron is trapped in conduction band, the angular momentum was partially transferred to the resonant $L_3M_{4,5}M_{4,5}$ Auger electrons instead.

As shown in Figure 5, the azimuthal intensity profiles of the [101] FFPs excited by CPL were individually fitted by Gaussians centered at $\phi = 2.89^\circ m_f$ directions corresponding to the different angular momenta of emitted electrons. Note that the photoelectrons from 3*d* valence band gain angular momentum σ by CPL excitation ($m_f = 3, 2, \sim -1$), while the angular momenta of *LMM* Auger electrons

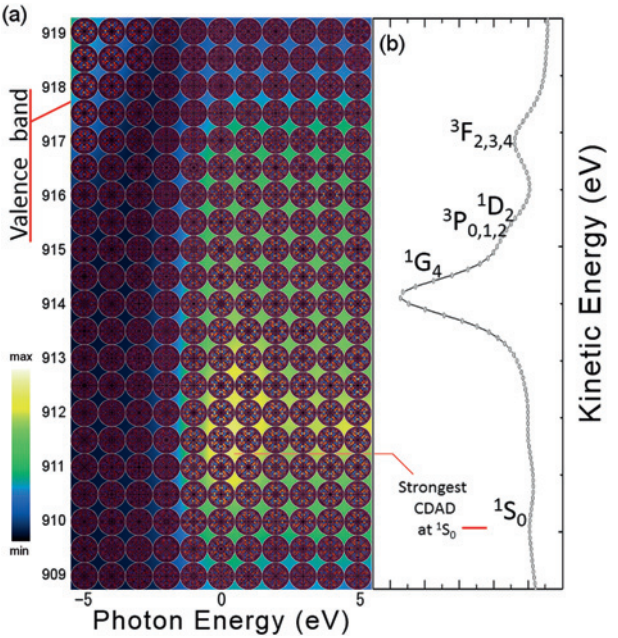

Figure 6: (a) Angular distributions of circular dichroism (CDAD) with different photon and kinetic energies at vicinity of L_3 absorption threshold. Photon energy relative to the L_3 absorption resonance is indicated. Each 2π steradian CDAD contrast was squared and averaged as indicated in the background according to the color bar in the left. (b) Corresponding Cu *LMM* Auger electron spectrum obtained by averaging for various photon energies at each kinetic energy.

are the same as those of $3d$ valence electrons ($m_i = \pm 2, \pm 1, 0$). The components of $m_f = \pm 3$ do not exist in the FFP of AIAD as shown in Figure 5. The origin of circular dichroism in the resonant AIAD at L_3 absorption threshold, where the excited core electron is trapped at conduction band, is attributed to the transition difference to the final states $m_f = \pm 1$ as well as ± 2.

4.3 Various two-hole final states

Details of the kinetic energy and photon energy dependence of circular dichroism were surveyed at the vicinity of the L_3 absorption edge. Figure 6(a) shows the CDAD contrasts measured using DIANA with the analyzer energy window width of 2 eV. The kinetic energy indicated here was about 1.5 eV larger than the actual value. The excitation photon energy relative to the absorption threshold is indicated. The corresponding Auger electron spectrum is shown in Figure 6(b). The Auger electron intensity was largest at 914 eV corresponding to the $^1G_4$ two-hole state, while the circular dichroism contrast was largest at 910 eV corresponding to the satellite peak of $^1S_0$ two-hole state. At the L_3 absorption threshold, $2p$ core electron is excited to $4s$ conduction band. Since the MQN of $4s$ state is 0, orbital-momentum-polarized core hole with $m_i = \mp 1$ is created by $\sigma = \pm 1$ excita-

tion. Several Auger decay paths with different final states exist. Final states with different energy can be selected by the energy analysis of Auger electron. The final state $^1S_0$ consists of two hole states having angular momentum with opposite sign ($m_A = -m_B$). When a valence electron with $m_A = -1$ decays to fill $2p$ ($m_i = -1$) core hole, another valence counterpart with $m_B = 1$ is emitted as $L_3M_{4,5}M_{4,5}$ Auger electron of $^1S_0$. Dipole operators Y_{10} and Y_{10}^* mediate these processes. The exchange term (Equation 11) is forbidden. When valence electrons with $m_A = -2$ and 0 decay, the counterparts will be the ones with $m_B = 2$ and 0, respectively. Since the angular momentum is conserved throughout whole process, an Auger electron with $m_f = 1$ is emitted by a $\sigma = 1$ excitation in the case of $^1S_0$ two-hole final state.

5 Conclusion

In conclusion, we have measured a full hemisphere intensity angular distribution of resonant $L_3M_{4,5}M_{4,5}$ Auger electrons excited by CPL, as well as that of $3d$ valence photoelectron. In the case of resonant Auger electrons where the excited core electron is trapped at the conduction band, the CDAD contrast was clearly observed. Moreover, from the kinetic energy dependence of Auger electron FFP parallax shift, we found that the angular momentum is transferred to the Auger electron most effectively in the case of the $^1S_0$ two-hole creation where two states involved have a same MQN but with opposite signs. This method has a great advantage in doping the hole states in valence band as compared to the simple valence band photoexcitation, especially in the case of compound crystals and thin films owing to the element selectivity and high sensitivity of Auger electron emission.

Acknowledgement: This work was performed with the approval of the Japan Synchrotron Radiation Research Institute (Proposals No. 2013B1307 and 2014B1454) and Paul Scherrer Institute. The authors deeply thank Mr. Rolf Wullschleger, Dr. Takayuki Muro, Dr. Tetsuya Nakamura, and Dr. Toyohiko Kinoshita for their support in the experiments. This research was supported by the Ministry of Education, Science, Sports and Culture, Grant-in-Aid for Scientific Research (B), 25287075, 2013 and JSPS Grant-in-Aid for Scientific Research on Innovative Areas "3D Active-Site Science": 26105007 2604. The experiment at Switzerland was supported by the Foundation for Nara Institute of Science and Technology.

Appendix

Gaunt Coefficient. Gaunt coefficient is proportional to the product of three spherical harmonics integrated over the full solid angle. It is easily derived from Clebsch-Gordan coefficients.

$$\langle l_\mathrm{f} m_\mathrm{f} | \nu\sigma | l_\mathrm{i} m_\mathrm{i} \rangle = \int_0^\pi \int_0^{2\pi} \sin\theta d\theta d\phi Y^*_{l_\mathrm{f},m_\mathrm{f}} Y_{\nu\sigma} Y_{l_\mathrm{i} m_\mathrm{i}} \tag{19}$$

$$= \sqrt{\frac{(2l_\mathrm{i}+1)(2\nu+1)}{4\pi(2l_\mathrm{f}+1)}} C(l_\mathrm{i}\nu l_\mathrm{f};000) C(l_\mathrm{i}\nu l_\mathrm{f};m_\mathrm{i}\sigma m_\mathrm{f}) \tag{20}$$

$$= \sqrt{\frac{2\nu+1}{4\pi}} c^\nu(l_\mathrm{f}, m_\mathrm{f}, l_\mathrm{i}, m_\mathrm{i}) \tag{21}$$

$\mathbf{s} \longrightarrow \mathbf{p} : l_\mathrm{i} = 0,\ l_\mathrm{f} = 1$

$c^1(1,\pm1,0,0) = 1/\sqrt{3}$

$c^1(1,0,0,0) = 1/\sqrt{3}$

$\mathbf{p} \longrightarrow \mathbf{s} : l_\mathrm{i} = 1,\ l_\mathrm{f} = 0$

$c^1(0,0,1,\pm1) = -1/\sqrt{3}$

$c^1(0,0,1,0) = 1/\sqrt{3}$

$\mathbf{p} \longrightarrow \mathbf{d} : l_\mathrm{i} = 1,\ l_\mathrm{f} = 2$

$c^1(2,\pm2,1,\pm1) = \sqrt{2/5}$

$c^1(2,\pm1,1,\pm1) = 1/\sqrt{5}$

$c^1(2,0,1,\pm1) = 1/\sqrt{15}$

$c^1(2,\pm1,1,0) = 1/\sqrt{5}$

$c^1(2,0,1,0) = 2/\sqrt{15}$

$\mathbf{d} \longrightarrow \mathbf{p} : l_\mathrm{i} = 2,\ l_\mathrm{f} = 1$

$c^1(1,\pm1,2,\pm2) = -\sqrt{2/5}$

$c^1(1,\pm1,2,\pm1) = 1/\sqrt{5}$

$c^1(1,\pm1,2,0) = -1/\sqrt{15}$

$c^1(1,0,2,\pm1) = -1/\sqrt{5}$

$c^1(1,0,2,0) = 2/\sqrt{15}$

$\mathbf{d} \longrightarrow \mathbf{f} : l_\mathrm{i} = 2,\ l_\mathrm{f} = 3$

$c^1(3,\pm3,2,\pm2) = \sqrt{3/7}$

$c^1(3,\pm2,2,\pm2) = 1/\sqrt{7}$

$c^1(3,\pm1,2,\pm2) = 1/\sqrt{35}$

$c^1(3,\pm2,2,\pm1) = \sqrt{2/7}$

$c^1(3,\pm1,2,\pm1) = 2\sqrt{2/35}$

$c^1(3,0,2,\pm1) = \sqrt{3/35}$

$c^1(3,\pm1,2,0) = \sqrt{6/35}$

$c^1(3,0,2,0) = 3/\sqrt{35}$

Transition probability. Transition probability from the initial state $(l_\mathrm{i}, m_\mathrm{i})$ to the final state $(l_\mathrm{f}, m_\mathrm{f})$ is the square of $C^1(l_\mathrm{f}, m_\mathrm{f}, l_\mathrm{i}, m_\mathrm{i})\Theta_{l_\mathrm{f}m_\mathrm{f}}$.

s → p :

$$c^1(1,\pm1,0,0)\Theta_{1\pm1} = \frac{\sin\theta}{2}$$

$$c^1(1,0,0,0)\Theta_{10} = \frac{\cos\theta}{\sqrt{2}}$$

p → s :

$$c^1(0,0,1,\pm1)\Theta_{00} = -\frac{1}{\sqrt{6}}$$

$$c^1(0,0,1,0)\Theta_{00} = \frac{1}{\sqrt{6}}$$

p → d :

$$c^1(2,\pm2,1,\pm1)\Theta_{2\pm2} = \frac{\sqrt{3}\sin^2\theta}{2\sqrt{2}}$$

$$c^1(2,\pm1,1,0)\Theta_{2\pm1} = \frac{\sqrt{3}\sin\theta\cos\theta}{2}$$

$$c^1(2,0,1,\mp1)\Theta_{20} = \frac{3\cos^2\theta - 1}{2\sqrt{6}}$$

$$c^1(2,\pm1,1,\pm1)\Theta_{2\pm1} = \frac{\sqrt{3}\sin\theta\cos\theta}{2}$$

$$c^1(2,0,1,0)\Theta_{20} = \frac{3\cos^2\theta - 1}{\sqrt{6}}$$

d → p :

$$c^1(1,\pm1,2,\pm2)\Theta_{1\pm1} = -\frac{\sqrt{3}\sin\theta}{\sqrt{10}}$$

$$c^1(1,0,2,\pm1)\Theta_{10} = -\frac{\sqrt{3}\cos\theta}{\sqrt{10}}$$

$$c^1(1,\mp1,2,0)\Theta_{1\mp1} = -\frac{\sin\theta}{2\sqrt{5}}$$

$$c^1(1,\pm1,2,\pm1)\Theta_{1\pm1} = \frac{\sqrt{3}\sin\theta}{2\sqrt{5}}$$

$$c^1(1,0,2,0)\Theta_{10} = \frac{\sqrt{2}\cos\theta}{\sqrt{5}}$$

d → f :

$$c^1(3,\pm3,2,\pm2)\Theta_{3\pm3} = \frac{\sqrt{30}}{8}\sin^3\theta$$

$$c^1(3,\pm2,2,\pm1)\Theta_{3\pm2} = \frac{\sqrt{30}}{4}\sin^2\theta\cos\theta$$

$$c^1(3,\pm1,2,0)\Theta_{3\pm1} = \frac{3}{4\sqrt{5}}\sin\theta\left(5\cos^2\theta - 1\right)$$

$$c^1(3,0,2,\mp1)\Theta_{3,0} = \frac{1}{2}\sqrt{\frac{3}{10}}\left(5\cos^3\theta - 3\cos\theta\right)$$

$$c^1(3,\mp1,2,\mp2)\Theta_{3,\mp1} = \frac{1}{4}\sqrt{\frac{3}{10}}\sin\theta\left(5\cos^2\theta - 1\right)$$

$$c^1(3,\pm2,2,\pm2)\Theta_{3\pm2} = \frac{\sqrt{15}}{4}\sin^2\theta\cos\theta$$

$$c^1(3,\pm1,2,\pm1)\Theta_{3\pm1} = \frac{1}{2}\sqrt{\frac{3}{5}}\sin\theta\left(5\cos^2\theta - 1\right)$$

$$c^1(3,0,2,0)\Theta_{30} = \frac{3}{2\sqrt{10}}\left(5\cos^3\theta - 3\cos\theta\right)$$

References

1. C. S. Fadley, J. Electron Spectrosc. **178–179** (2010) 2.
2. S. Kono, S. M. Goldberg, N. F. T. Hall, C. S. Fadley, Phys. Rev. B **22** (1980) 6085.
3. W. F. Egelhoff Jr., Phys. Rev. B **30** (1984) 1052.
4. H. C. Poon and S. Y. Tong, Phys. Rev. B **30** (1984) 6211.
5. H. Daimon, Phys. Rev. Lett. **86** (2001) 2034.
6. F. Matsui, T. Matsushita, Y. Kato, F. Z. Guo, and H. Daimon, J. Phys. Soc. Jpn. **76** (2007) 013705.
7. K. Goto, F. Matsui, T. Matsushita, Y. Kato, and H. Daimon, J. Phys. Soc. Jpn. **77** (2008) 103301.
8. F. Matsui, M. Fujita, T. Ohta, N. Maejima, H. Matsui, H. Nishikawa, T. Matsushita, and H. Daimon, Phys. Rev. Lett. **114** (2015) 015501.
9. S. M. Goldberg, C. S. Fadley, and S. Kono, J. Electron Spectrosc. **21** (1981) 285.
10. J. A. Gaunt, Trans. Roy. Soc. London **A228** (1928) 195.
11. T. Greber, J. Phys.-Condens. Mat. **13** (2001) 10561.
12. F. Matsui, H. Miyata, O. Rader, Y. Hamada, Y. Nakamura, K. Nakanishi, K. Ogawa, H. Namba, and H. Daimon, Phys. Rev. B **72** (2005) 195417.
13. H. Daimon, S. Imada, and S. Suga, Surf. Sci. **471** (2001) 143.
14. http://sourceforge.jp/projects/tmcoca/.
15. H. Daimon, T. Nakatani, S. Imada, S. Suga, Y. Kagoshima, and T. Miyahara, Jpn. J. Appl. Phys. **32** (1993) L1480.
16. F. Matsui, T. Matsushita, and H. Daimon, J. Electron Spectrosc. **178–179** (2010) 221.
17. F. Matsui, N. Nishikayama, N. Maejima, H. Matsui, K. Goto, M. Hashimoto, T. Hatayama, T. Matsushita, Y. Kato, and H. Daimon, J. Phys. Soc. Jpn. **80** (2011) 013601.
18. V. O. Kostroum, M. H. Chen, and B. Crasemann, Phys. Rev. A **3** (1971) 533.
19. W. Bambynek, B. Crasemann, R. W. Fink, H.-U. Freund, H. Mark, C. D. Swift, R. E. Price, and P. Venugopara Rao, Rev. Mod. Phys. **44** (1972) 716.
20. E. Antonides, E. C. Janse, and G. A. Sawatzky, Phys. Rev. B **15** (1977) 1669.
21. P. J. Feibelman, and E. J. McGuire, Phys. Rev. B **15** (1977) 3575.
22. E. J. McGuire, Phys. Rev. A **17** (1978) 182.
23. S. Aksela and J. Sivonen, Phys. Rev. A **25** (1982) 1243.
24. T. Matsushita, F. Z. Guo, F. Matsui, Y. Kato, and H. Daimon, Phys. Rev. B **75** (2007) 085419.
25. F. Matsui, T. Matsushita, Y. Kato, M. Hashimoto, K. Inaji, F. Z. Guo, and H. Daimon, Phys. Rev. Lett. **100** (2008) 207201.
26. P. Oberta, U. Flechsig, M. Muntwiler, and C. Quitmann, Nucl. Instrum. Methods **A635** (2011) 116.
27. H. Daimon, Rev. Sci. Instrum. **59** (1988) 545.
28. M. Kotsugi, Y. Miyatake, K. Enomoto, K. Fukumoto, A. Kobayashi, T. Nakatani, Y. Saitoh, T. Matsushita, S. Imada, T. Furuhata, S. Suga, K. Soda, M. Jinno, T. Hirano, K. Hattori, and H. Daimon, Nucl. Instrum. Methods **A467–A468** (2001) 1493.
29. Y. Saitoh, H. Kimura, Y. Suzuki, T. Nakatani, T. Matsushita, T. Muro, T. Miyahara, M. Fujisawa, K. Soda, S. Ueda, H. Harada, M. Kotsugi, A. Sekiyama, and S. Suga, Rev. Sci. Instrum. **71** (2000) 3254.
30. F. Matsui, T. Matsushita, and H. Daimon, J. Electron Spectrosc. **195** (2014) 347.

31. T. Muro, T. Nakamura, T. Matsushita, H. Kimura, T. Nakatani, T. Hirono, T. Kudo, K. Kobayashi, Y. Saitoh, M. Takeuchi, T. Hara, K. Shirasawa, and H. Kitamura, J. Electron Spectrosc. **144–147** (2005) 1101.
32. I. Coulthard, T. K. Sham, Y.-F. Hu, S. J. Naftel, P.-S. Kim, and J. W. Freeland, Phys. Rev. B **64** (2001) 115101.
33. A. Föhlisch, O. Karis, M. Weinelt, J. Hasselström, A. Nilsson, and N. Mårtensson, Phys. Rev. Lett. **88** (2001) 027601.
34. H. H. Madden, D. M. Zehner, and J. R. Noonan, Phys. Rev. B **17** (1978) 3074.
35. H. W. Haak, G. A. Sawatzky, and T. D. Thomas, Phys. Rev. Lett. **41** (1978) 1825.
36. C. P. Lund, S. M. Thurgate, and A. B. Wedding, Phys. Rev. B **55** (1997) 5455.
37. M. Magnuson, N. Wassdahl, and J. Nordgren, Phys. Rev. B **56** (1997) 12238.
38. L. C. Davis and L. A. Feldkamp, Phys. Rev. B **23** (1981) 6239.
39. N. Mårtemsson and B. Johansson, Phys. Rev. B **28** (1983) 3733.
40. M. Morscher, F. Nolting, T. Brugger, and T. Greber, Phys. Rev. B **84** (2011) 140406(R).